WJRS LETTERS

For rapid publication of innovative, leading-edge research on joining and additive manufacturing topics in the *Welding Journal Research Supplement*

Rotary Inertia Friction Welding of Dissimilar High-Strength 422 Martensitic Stainless Steel and 4140 Low Alloy Steel for Heavy-Duty Engine Piston Fabrication

As-welded dissimilar 422/4140 rotary inertia friction welding joints were characterized in detail

BY Y. WANG, K. SEBECK, M. TESS, E. GINGRICH, M. J. LANCE, J. A. HAYNES, Z. FENG, AND D. PIERCE

■ **Keywords:** 422 martensitic stainless steel, 4140 low alloy steel, dissimilar metal joint, inertial rotary friction welding, interfacial microstructure, mechanical properties

Introduction

AISI 422 martensitic stainless steel with superior high-temperature performance (oxidation resistance and strength) is under evaluation for replacing current heavy-duty piston crown materials, AISI 4140 martensitic steel and microalloyed steel (MAS) 38MnSiVS5, to fabricate a multimaterial piston (Refs. 1, 2). This multimaterial piston concept further improved power density and fuel economy by allowing heavy-duty diesel engines to operate at higher temperatures and pressures (Ref. 3). Joining AISI 422 steel piston crowns with AISI 4140 steel piston skirts is a key manufacturing step for this multimaterial piston. However, the significant differences in strength, elevated temperature flow stress, alloy chemistry, and temper resistance between these two martensitic steels cause some weldability issues (cracking) and metallurgical challenges (alloying element migration/segregation) when using conventional fusion-based welding processes (Refs. 4–6). Rotary inertia friction welding (RIFW), a solid-state welding process, has been the preferred method to join 4140 crowns to 4140 skirts (and MAS crowns to MAS skirts) in high-volume production of current heavy-duty diesel engine pistons. It has been used to join these two materials with relatively comparable alloy chemistry to fabricate pistons with MAS skirts and 4140 crowns. Meanwhile, RIFW has also been a preferred method of dissimilar metal welding (Refs. 7, 8). However, RIFW of dissimilar high-strength martensitic steels has yet to be widely pursued. The interfacial microstructure complexities created by the thermomechanical process and highly nonequilibrium phase transformations during RIFW are a significant challenge for understanding and predicting their joining behavior and have not been reported in detail. In this work, defect-free AISI 422 steel-AISI 4140 multimaterial pistons were successfully fabricated using the RIFW process. The interfacial microstructure and mechanical properties of dissimilar 422/4140 steel RIFW in the as-welded condition were experimentally studied in detail. The results provide critical baseline information for understanding RIFW mechanisms and guiding subsequent postweld heat treatment (PWHT) practice.

Experimental Procedures

4140 martensitic low-alloy steel and 422 martensitic stainless steel were used as the base metals (BMs) of the piston skirt and crown, respectively. The chemical compositions of both steel BMs were reported in an earlier work (Ref. 9). The two steels were normalized and tempered to hardnesses of 33 HRC (422) and 30 HRC (4140). The 422 piston crowns and 4140 skirts were joined with an RIFW machine (Rotary Friction Welder, Manufacturing Technology Inc.). The forged 4140 piston skirt was held in the nonrotating vice, and the machined 422 piston crown was held in the rotating chuck. The controlled welding parameters included a moment of inertia (~ 919 lb/ft^2), initial rotational speed (~ 1393–1425 rpm), and specific load, which resulted in material flash and an upset. Fig. 1 shows an example of the cross section of a 422-4140 welded piston before final machining. Fig. 1B shows that two welds (a small inner weld and a larger outer weld) were produced simultaneously in this piston design. In contrast to the earlier work in (Ref. 9), the piston weld was analyzed and tested in the as-welded condition (without PWHT) in this current work.

Metallurgical specimens (inner and outer) were extracted from the as-welded piston. The mechanical-polished specimens were etched with Glyceregia etchant. Multiscale microstructural analyses were performed with a Keyence VHX-6000 digital optical microscope and a TESCAN MIRA3 XMH Schottky field emission scanning electron microscope (SEM) equipped with EDAX energy-dispersive x-ray (EDS), EDAX electron backscatter diffraction (EBSD), and backscatter electron (BSE) detector. Compositional analyses across the weld interface were acquired on an electron microprobe

https://doi.org/10.29391/2025.104.007

analyzer (EPMA, JEOL 8200). The accelerating voltage was set to 20.0 kV, and the beam current was 50.0 nA.

Microhardness (Vickers) mapping with a load of 0.1 kgf with a dwell time of 10 s and an interspacing of 0.15 mm was conducted on the as-polished metallurgical specimens. Sub-scale tensile specimens were extracted from the outer and inner welds such that the weld line was perpendicular to the specimen axis and in the center of the specimen (Ref. 9). Sub-sized specimens with a 28.3 mm overall length, 9.5 mm gauge length, 2.0 mm gauge width, and 2.0 mm gauge thickness were used for tensile testing. Tensile testing at a strain rate of 0.001 s^{-1} was performed at room temperature. Fractography analysis was also conducted on a fractured specimen after tensile tests using optical and SEM microscopes.

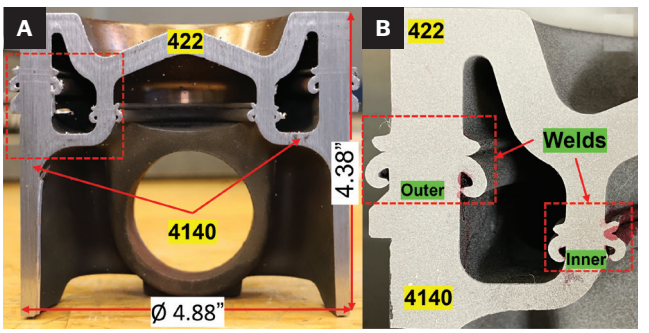

Fig. 1 — A — An example of the cross section of the welded piston with 422 crown and 4140 skirt (Ref. 9); B — two friction welds, outer weld (left) and inner weld (right), are highlighted.

Results and Discussion

Dye penetrant and phased array ultrasonic examinations and microstructural analysis were conducted on the 422/4140 piston welds, with results indicating no common defects (cracks, lack of fusion, or porosity) detected in the piston welds. Cross sections of the as-welded outer and inner welds are shown in Figs. 2A and B, respectively, showed a sound metallurgical bond formed without defects between the 422 and 4140 steels. The two steels' very different compositions, elevated temperature strengths, and flow stresses resulted in different material flow and asymmetric flash formation on the edges. The lower elevated temperature strength and lower flow stress of the 4140 resulted in

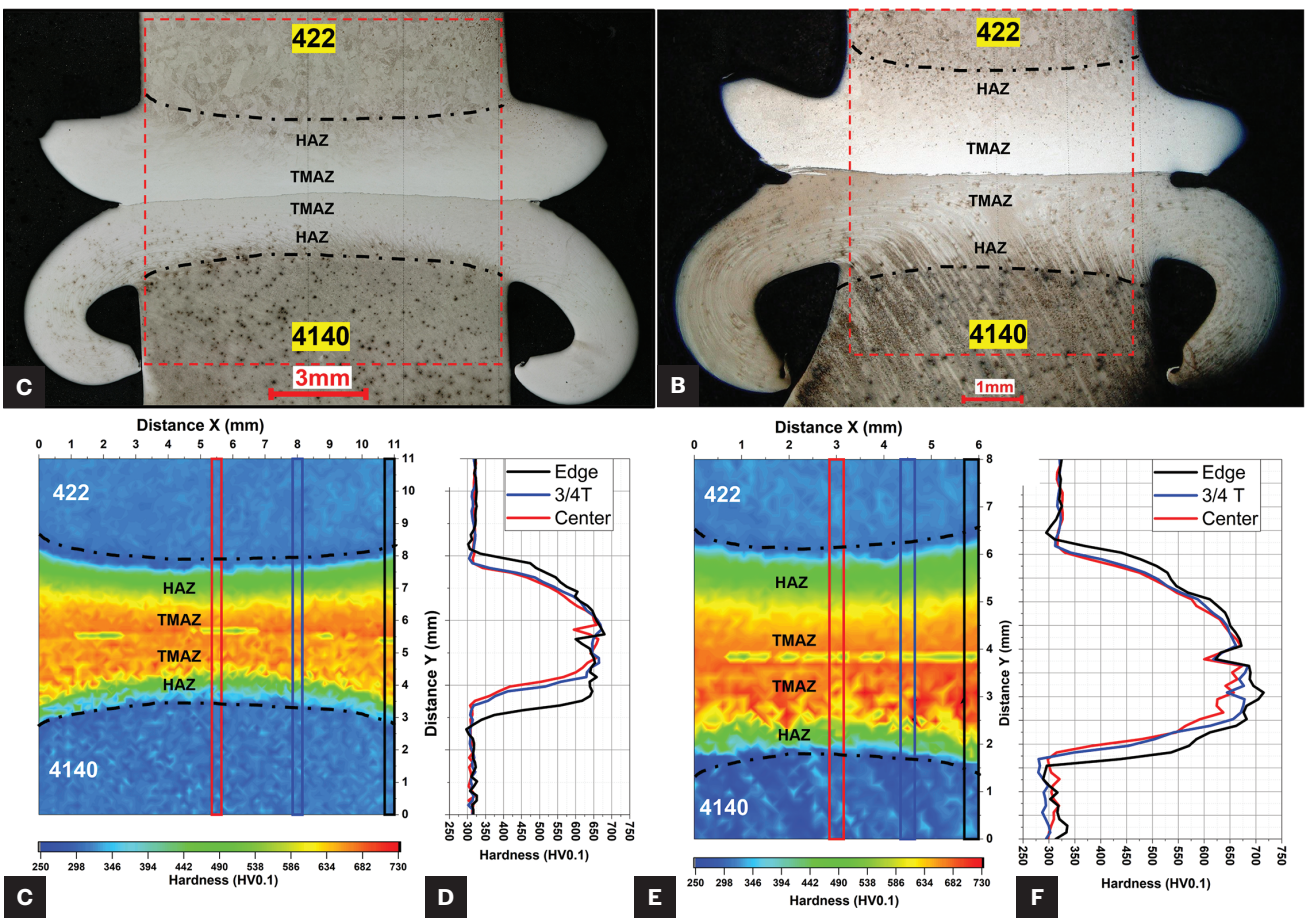

Fig. 2 — A and B — Optical images showing the macro-structure of the 422/4140 outer and inner welds, respectively. The locations of hardness maps are marked by red boxes; C and E — hardness distribution contour maps of the marked regions in A and B, respectively; D and F — hardness line profiles corresponding to the locations indicated by the vertical-colored boxes in C and E. Note: Distance scales are different in C/D and E/F.

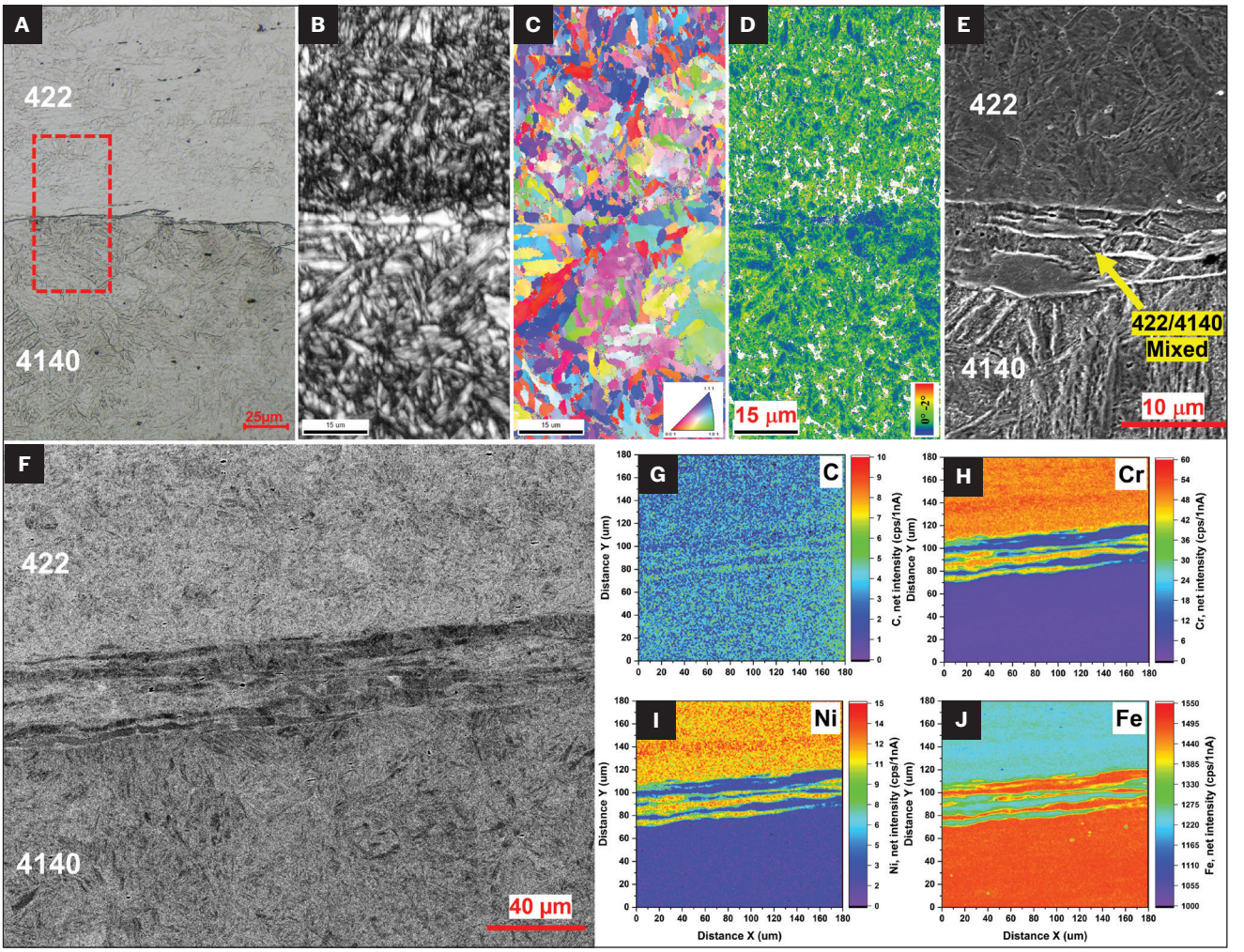

Fig. 3 — Interfacial microstructure of the as-welded 422/4140 outer weld: A — Optical image; B–D — EBSD data obtained from the region marked by the red box in A; B — image quality map; C — inverse pole figure; D — kernel average misorientation map (0–2 deg). The white regions in D are regions with KAM values beyond 2 deg; E — secondary-electron SEM image of weld interface; F — BSE SEM image of the as-polished weld interface for EPMA composition analysis; G–J — EPMA element maps (C, Cr, Fe, Ni). EPMA maps are net intensity maps.

more material flow and a larger flash. In contrast, the 422, with greater elevated temperature strength and flow stress, had much less material flow. Figs. 2C–2F show the hardness distributions across the outer and inner welds. Based on the microstructure and hardness distribution, this RIFW joint consists of a thermal-mechanical affected zone (TMAZ) and a heat-affected zone (HAZ) on each side of the interface. The total width of the TMAZ and HAZ on the 422 side was slightly larger than that on the 4140 side. A sharp hardness transition (~ 300–700 HV) formed from the parent materials to the weld interface. The TMAZs exhibited the highest hardness (max. 700 HV), followed by the HAZ (300–600 HV). Note that there were a few relatively soft regions with a hardness of 450–575 HV located at the interface, as shown in Fig. 2C and E. Characterization showed a mixing of the 422 and 4140 materials at these relatively soft regions.

Fig. 3 presents more details of the interfacial TMAZ microstructure of the outer weld. Overall, a clear interface between the 422 and 4140 was visible in some regions of the joint, but at some local regions, mixing occurred between the two steels at the interface. The inner weld had a larger portion of regions where 422 and 4140 were mixed relative to the outer weld. Typical martensitic microstructures were observed on both TMAZ sides, indicating the microstructure was austenitized due to the heat generated during the welding and then rapidly cooled, which along with the high hardenability of both BMs, resulted in martensite formation.

The EBSD image quality map in Fig. 3B shows a fine microstructure with small martensite blocks (average block size: 5 μm) formed in the 422-TMAZ. Longer and wider martensite blocks (average size: 10 μm) were observed in the 4140-TMAZ. This block size difference is likely related to a larger prior austenite grain of 4140 caused by lower thermal stability relative to 422. During the RIFW process, the peak temperature in the TMAZ increased above the critical A3 temperature, causing austenitization on heating, and martensitic transformation on cooling. No obvious texture (preferred orientation) was formed in either TMAZ, as shown

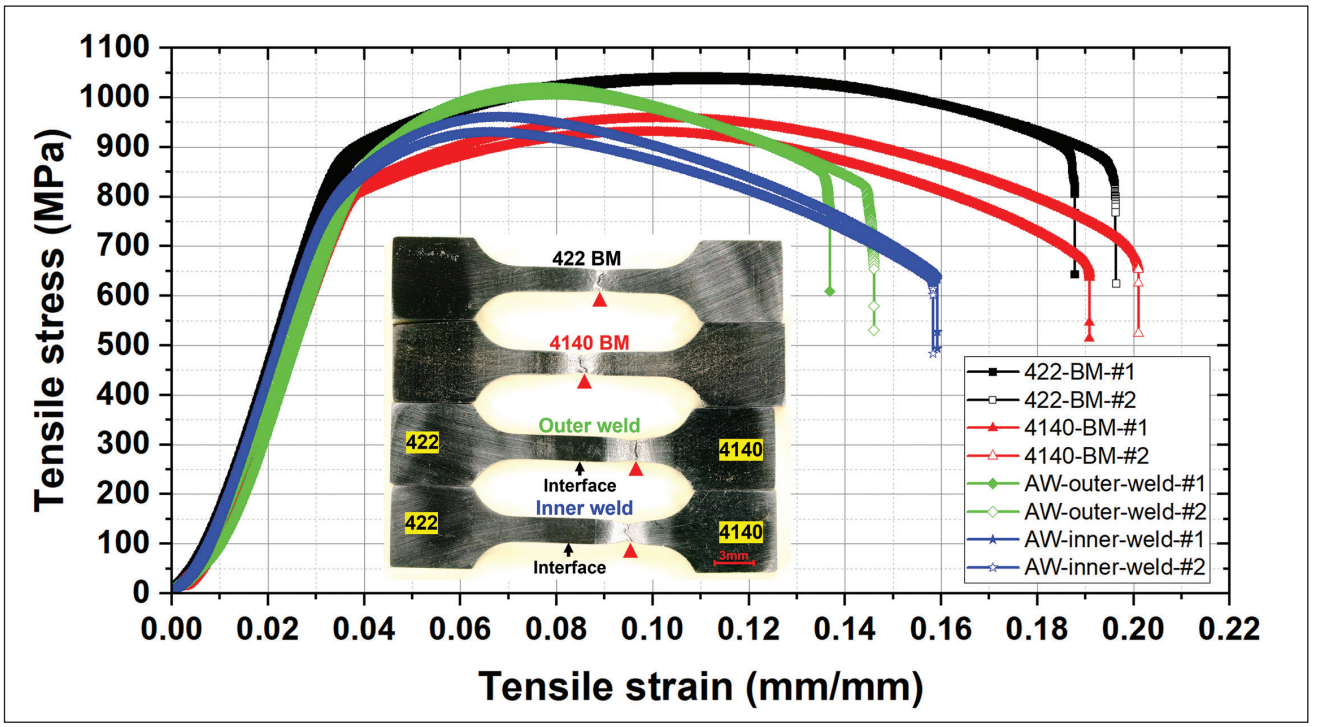

Fig. 4 — Tensile stress-strain curves of subsize tensile specimens (BMs and welds) extracted from the as-welded piston. Photos of the fractured specimens show the fracture locations.

Table 1 — Average Measured Tensile Properties for the 422 BM, 4140 BM, Outer Weld, and Inner Weld

Specimen	Yield Strength (MPa)	Ultimate Tensile Strength (MPa)	Strain at Fracture (%)	Fracture Location
422 BM	874 ± 18	1040 ± 22	19.2 ± 0.7	Gauge
4140 BM	800 ± 18	944 ± 22	19.6 ± 0.7	Gauge
Outer Weld	830 ± 18	1014 ± 22	14.1 ± 0.7	4140 BM
Inner Weld	789 ± 18	946 ± 22	15.9 ± 0.7	4140 BM

Note: The YS was determined by the 0.2% offset strain method using the approximately linear portion of the stress strain curve from ~ 0.01–0.03 strain. The use of subscale specimens and cross head displacement in this work may introduce additional systematic errors.

by the EBSD inverse pole figure in Fig. 3C. The KAM map in Fig. 3D indicates a high localized strain due to martensite formation. The coarser blocky grains on the 4140 side showed modestly lower strain. The SEM image in Fig. 3E shows a region where mixing occurred, as evidenced by islands of 422 in the 4140 matrix. EPMA mapping analyses (Figs. 3G–3J) of the mixed region indicated in Fig. 3F reveals an interface microstructure comprised of alternating layers of 422 and 4140. Clear boundaries of 422 and 4140 constituents were traceable based on the Cr, Fe, and Ni maps in Figs. 3H–3J, suggesting that long-range diffusion of Cr, Ni, or Fe was limited during welding. The carbon intensity map in Fig. 3G shows slightly higher carbon intensities on the 4140 side away from the interface compared to the 422 side away from the interface, originating from the greater carbon content of 4140 (0.44 wt-%) compared to 422 (0.23 wt-%). In the 422-4140 material system, C diffusion from 4140 to 422 is favored. However, the carbon intensity map suggested limited C diffusion from 4140 to 422 occurs during welding, with the possible exception of slight C enrichment in the horizontal layers of 422 material located within the 4140 matrix. The lack of significant migration of alloying elements detected at the interface is likely related to the high heating and cooling rates of the RIFW process, the short time the interface

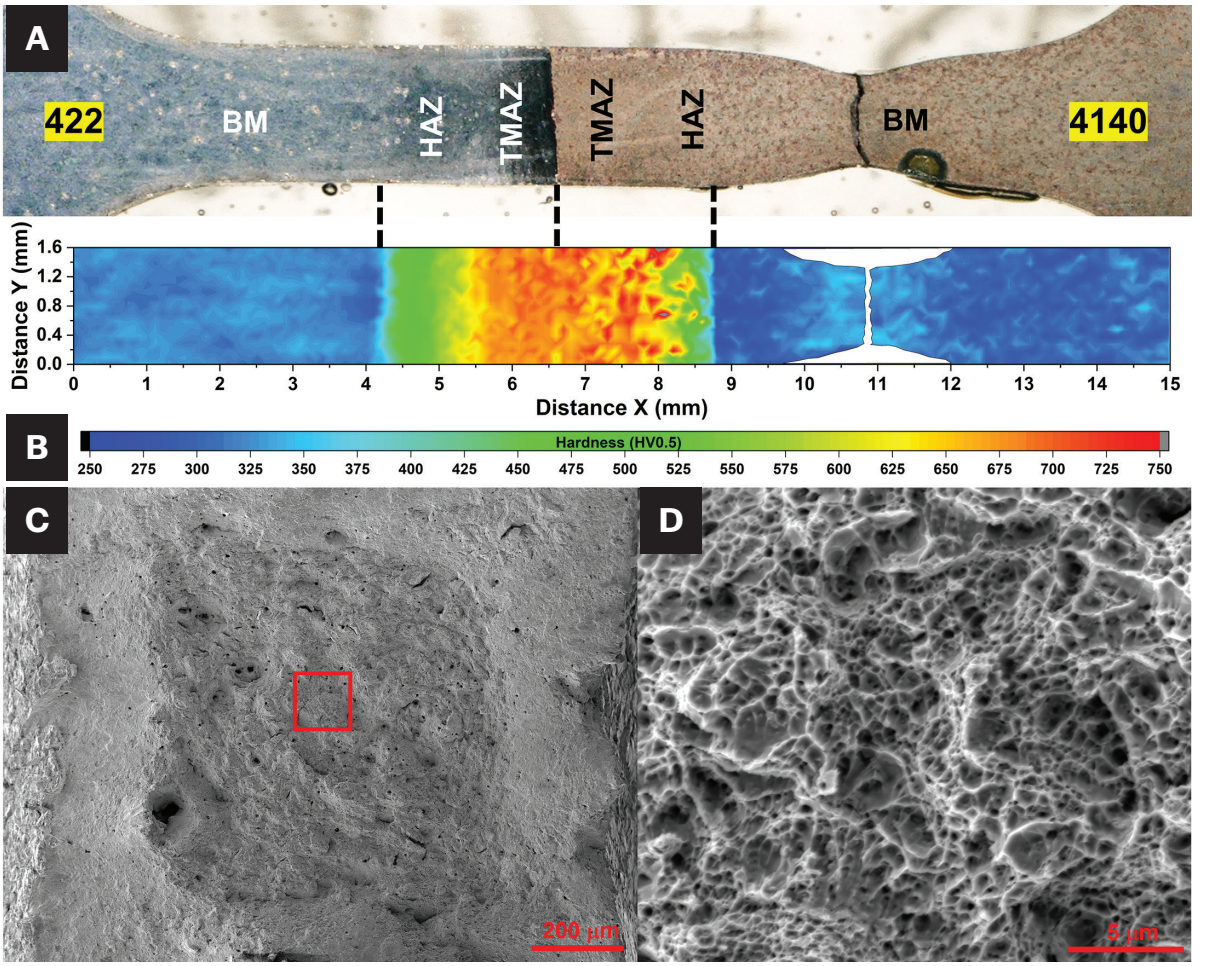

Fig. 5 — A — Optical image of a fractured tensile specimen from the as-welded 422/4140 inner weld; B — hardness distribution contour map; C and D — SEM images show fractography of the fractured tensile specimen.

was at high temperatures, and the continual introduction of new material into the interface followed by ejection into the weld flash.

Fig. 4 plots stress-strain curves of the tested subsized tensile specimens of the BMs and welds. Their tensile properties are summarized in Table 1. The BMs and welds exhibited quite different tensile properties. The 422 BM has the highest yield strength (YS) and ultimate tensile strength (UTS), while the strength of 4140 BM was considerably lower. The "weld properties" reflect a composite of the BMs, TMAZs, and HAZs on each side of the interface included in the gauge length of the tensile specimen. Both inner and outer welds fractured in the 4140 BM, not along the weld interface during tensile deformation, indicating the weld interfaces are resistant to the imposed stress levels. The asymmetry in the strength levels of the two BMs, along with the hard martensite in the TMAZ and HAZ (apparently tends to concentrate tensile deformation), ultimately led to failure in the 4140 BM. As such, the inner and outer weld specimens exhibit YSs significantly lower than the 422 BM and similar to the 4140 BM. Notably, the inner weld showed a lower strength compared to the outer weld, which may be due to the reduced strength of the 4140 BM near the inner weld HAZ as compared to the outer weld, as is observed in the hardness maps of Figs. 2C and E. The strength difference could be due to several factors. The linear velocity of the outer weld was significantly greater than the inner weld during the RIFW because of the piston geometry, and the thicknesses are also different, as shown in Figs. 2A and B, which may contribute to different thermal histories, microstructure, and properties. The photograph of the fractured specimens in Fig. 4 shows that necking occurred on the 4140 side of the welds.

Metallurgical analysis in Fig. 5A further confirmed the deformation is mainly localized on the 4140 side in the BM, while very limited deformation occurred on the 422 side. Hardness mapping in Fig. 5B showed that the TMAZ and HAZ each maintained high hardness values. There was likely relatively small deformation in the TMAZ and HAZ due to their untempered martensite microstructures. SEM images of the fracture surface of a failed weld specimen in Figs. 5C and D show the specimen fractured in a ductile mode with fine dimples on the fracture surface. The 4140 BM, instead of the weld interface, was the weakest link across the joint under the tensile load. Sharp hardness gradient across the weld, like that in Fig. 2, induces lower toughness in rotary friction welded joints (Refs. 10–12). A PWHT may beneficially reduce the high hardness transition across the weld and improve its toughness (Refs. 13, 14).

Conclusions

In this work, AISI 422 martensitic stainless steel was successfully joined with AISI 4140 steel using rotary inertia friction welding to fabricate a multimaterial piston. Characterization showed a sound metallurgical bonding without weld defects (porosity, cracks, etc.) formed between the 422 steel and 4140 steel. Fresh martensite was formed in the TMAZ and HAZ in both steels, resulting in large hardness gradients (700-300 HV) from the weld interface to the base metals. The chemical analysis showed no significant alloying element diffusion across the interface, with the exception of modest C enrichment in some local regions of 422. During tensile deformation, the 422/4140 RIFW joint failed away from the interface in the 4140 base metal in a ductile mode, indicating the joint interface can withstand high static stresses. Follow-up work will focus on methods to improve the ductility and toughness of the weld interface through optimization of weld parameters and PWHT. While significantly different tempering resistances between 4140 and 422 and a strong driving force for C diffusion between the steels create challenges in selecting PWHT parameters, an optimized PWHT should help improve the mechanical properties of the weld interface.

Acknowledgments

The authors acknowledge Cody Taylor, Jessica Osborne, and Jeremy Stidham for their technical support. The research was in part sponsored by the Powertrain Materials Core Program, under the Powertrain Materials Core Program (managed by Jerry Gibbs) in the Department of Energy, Vehicle Technologies Office, United States. The information, data, or work presented herein was conducted in part as an Advanced Vehicle Power Technology Alliance (AVPTA) "Extended Enterprise" project funded by the U.S. Army Ground Vehicle Systems Center (GVSC), U.S. Department of Defense, Department of the Army. AVPTA is chartered under the U.S. Department of Energy/U.S. Department of Defense Memorandum of Understanding titled "Concerning Cooperation in a Strategic Partnership to Enhance Energy Security." The research and development work was performed at the Oak Ridge National Laboratory, which is managed by UT-Battelle LLC for the U.S. Department of Energy under contract DE-AC05-00OR22725. The piston fabrication and welding were conducted by Tenneco and Manufacturing Technology Inc. The authors would also like to thank Jian Chen and Yong Chae Lim for the useful discussion and technical review.

References

1. Pierce, D., Haynes, J. A., Hughes, J., Graves, R. Maziasz, P., Muralidharan, G., Shyam, A., Wang, B., England, R., and Daniel, C. 2019. High temperature materials for heavy duty diesel engines: Historical and future trends. *Progress in Materials Science* 103: 109–179.

2. Gingrich, E., Pierce, D., Byrd, G., Sebeck, K., Korivi, V., Muralidharan, G., Wang, H., Torres, J., Trofimov, A., and Haynes, J. 2022. Evaluation of high-temperature martensitic steels for heavy-duty diesel piston applications. SAE Technical Paper.

3. Pierce, D., Muralidharan, G., Trofimov, A., Torres, J., Wang, H., Haynes, J. A., Sebeck, K., Gingrich, E., Byrd, G., and Tess, M. 2022. Evaluation of thermal processing and properties of 422 martensitic stainless steel for replacement of 4140 steel in diesel engine pistons. *Materials & Design* 214: 110373.

4. Folkhard, E. 2012. Welding metallurgy of stainless steels. *Springer Science & Business Media*.

5. Li, W., Vairis, A., Preuss, M., and Ma, T. 2016. Linear and rotary friction welding review. *International Materials Reviews* 61(2): 71–100.

6. Kou, S. 2003. *Welding Metallurgy*. Hoboken, N.J.: John Wiley & Sons.

7. Alves, E. P., Piorino, F., and An, C. Y. 2010. Welding of AA1050 aluminum with AISI 304 stainless steel by rotary friction welding process. *Journal of Aerospace Technology and Management* 2(3): 301–306.

8. Wang, G., Li, J., Wang, W., Xiong, J., and Zhang, F. 2018. Study on the effect of energy-input on the joint mechanical properties of rotary friction-welding. *Metals* 8(11): 908.

9. Wang, Y., Sebeck, K., Tess, M., Gingrich, E., Feng, Z., Haynes, J. A., Lance, M. J., Muralidharan, G., Marchel, R., Kirste, T., and Pierce, D. 2023. Interfacial microstructure and mechanical properties of rotary inertia friction welded dissimilar 422 martensitic stainless steel to 4140 low alloy steel joints. *Materials Science and Engineering: A* 885: 145607.

10. Saju, T., and Velu, M. 2022. Fracture toughness and fatigue crack growth rate studies on rotary friction weldments of nickel-based superalloys. *Materials Letters* 327: 133027.

11. Kumar, A. S., Khadeer, S. A., Rajinikanth, V., Pahari, S., and Kumar, B. R. 2021. Evaluation of bond interface characteristics of rotary friction welded carbon steel to low alloy steel pipe joints. *Materials Science and Engineering: A* 824: 141844.

12. Priymak, E., Boumerzoug, Z., Stepanchukova, A., and Ji, V. 2020. Residual stresses and microstructural features of rotary-friction-welded from dissimilar medium carbon steels. *Physics of Metals and Metallography* 121: 1339–1346.

13. Dong, H., Yang, J., Li, Y., Xia, Y., Hao, X., Li, P., Sun, D., Hu, J., Zhou, W., and Lei, M. 2020. Evolution of interface and tensile properties in 5052 aluminum alloy/304 stainless steel rotary friction welded joint after post-weld heat treatment. *Journal of Manufacturing Processes* 51: 142–150.

14. Mahajan, A. M., Babu, N. K., Talari, M. K., Rehman, A. U., and Srirangam, P. 2023. Effect of heat treatment on the microstructure and mechanical properties of rotary friction welded AA7075 and AA5083 dissimilar joint. *Materials* 16: 2464.

YIYU WANG (*wangy4@ornl.*gov), **MICHAEL J. LANCE**, **JAMES ALLEN HAYNES**, **ZHILI FENG**, and **DEAN PIERCE** (*dpierce@ornl.gov*) are research scientists from the Materials Science and Technology Division at Oak Ridge National Laboratory, Oak Ridge, Tenn. **KATHERINE SEBECK**, **MICHAEL TESS**, and **ERIC GINGRICH** are research engineers from the U.S. Army Combat Capabilities Development Command Ground Vehicle Systems Center, Warren, Mich.